

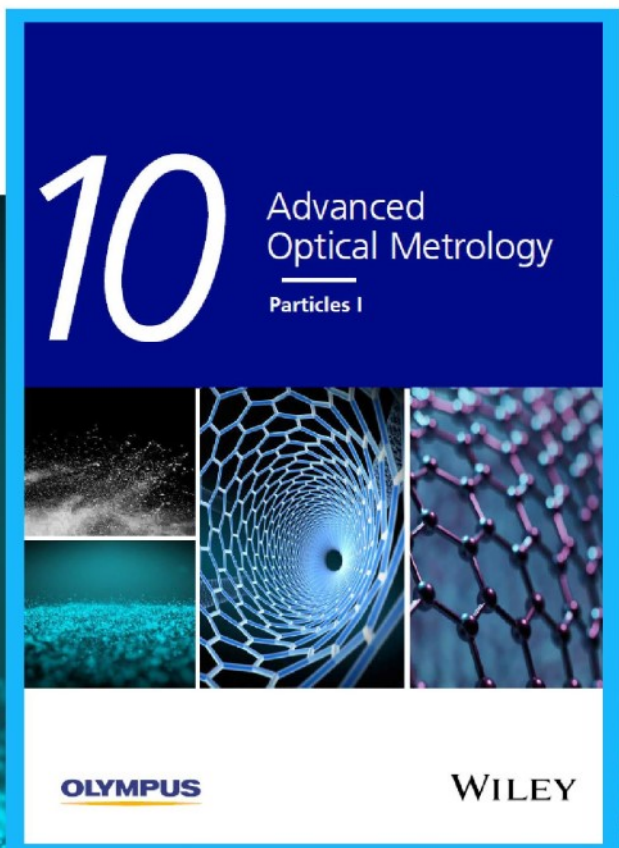


Particles I

Access the latest eBook →

Particles: Unique Properties,
Uncountable Applications

**Read the latest eBook and
better your knowledge with
highlights from the recent
studies on the design and
characterization of micro-
and nanoparticles for
different application areas.**



Access Now

This eBook is sponsored by

OLYMPUS

WILEY

2D Molybdenum Carbide MXenes for Enhanced Selective Detection of Humidity in Air

Hanna Pazniak,* Alexey S. Varezchnikov, Dmitry A. Kolosov, Ilya A. Plugin, Alessia Di Vito, Olga E. Glukhova, Polina M. Sheverdyeva, Marina Spasova, Igor Kaikov, Evgeny A. Kolesnikov, Paolo Moras, Alexey M. Bainyashev, Maksim A. Solomatin, Ilya Kiselev, Ulf Wiedwald, and Victor V. Sysoev*

2D transition metal carbides and nitrides (MXenes) open up novel opportunities in gas sensing with high sensitivity at room temperature. Herein, 2D Mo_2CT_x flakes with high aspect ratio are successfully synthesized. The chemiresistive effect in a sub- μm MXene multilayer for different organic vapors and humidity at 10^1 – 10^4 ppm in dry air is studied. Reasonably, the low-noise resistance signal allows the detection of H_2O down to 10 ppm. Moreover, humidity suppresses the response of Mo_2CT_x to organic analytes due to the blocking of adsorption active sites. By measuring the impedance of MXene layers as a function of ac frequency in the 10^{-2} – 10^6 Hz range, it is shown that operation principle of the sensor is dominated by resistance change rather than capacitance variations. The sensor transfer function allows to conclude that the Mo_2CT_x chemiresistance is mainly originating from electron transport through interflake potential barriers with heights up to 0.2 eV. Density functional theory calculations, elucidating the Mo_2C surface interaction with organic analytes and H_2O , explain the experimental data as an energy shift of the density of states under the analyte's adsorption which induces increasing electrical resistance.

industrial, medical, and environmental monitoring.^[1–3] Their advanced sensing capabilities result from an intrinsically high surface-to-volume ratio and easily tunable surface properties by functionalization.^[1,4] Following the impetus of graphene as a benchmark 2D material able to detect single molecules from a gaseous phase^[5] there is an enormous call for comprehensive gas-sensing options with a continuously growing number of 2D materials, like the transition metal dichalcogenides,^[6] hexagonal boron nitrides,^[7] metal–organic frameworks,^[8] or phosphorenes^[9] to name a few. Recently, this family has been expanded by MXenes, transition metal carbides, and nitrides $\text{M}_{n+1}\text{X}_n\text{T}_x$ with $n = 1, 2, 3$. Here, M represents an early transition metal, X is either carbon or nitrogen, and T_x formalize the surface functional groups, which are $-\text{F}$, $-\text{O}$, and/or $-\text{OH}$ as most frequent terminations.

Other T_x groups like $-\text{Cl}/-\text{O}^{[10]}$ and $-\text{Br}/-\text{O}^{[11]}$ have been recently demonstrated. MXenes appear in a 2D layered morphology which is noted by many authors as uniquely beneficial for gas-sensing applications combining this feature with


1. Introduction

2D materials are very promising materials to meet the demands of next-generation gas-sensing and gas-analytical platforms for

H. Pazniak, M. Spasova, U. Wiedwald
Faculty of Physics and Center for Nanointegration Duisburg-Essen
University of Duisburg-Essen
Lotharstr. 1, 47057 Duisburg, Germany
E-mail: hanna.pazniak@uni-due.de

A. S. Varezchnikov, I. A. Plugin, A. M. Bainyashev, M. A. Solomatin,
V. V. Sysoev
Yuri Gagarin State Technical University of Saratov
Politekhnikheskaya str. 77, Saratov 410054, Russia
E-mail: vsysoev@sstu.ru

D. A. Kolosov, O. E. Glukhova
Department of Physics
Saratov State University
Astrakhanskaya str. 83, Saratov 410012, Russia

 The ORCID identification number(s) for the author(s) of this article can be found under <https://doi.org/10.1002/adma.202104878>.

© 2021 The Authors. Advanced Materials published by Wiley-VCH GmbH. This is an open access article under the terms of the Creative Commons Attribution-NonCommercial-NoDerivs License, which permits use and distribution in any medium, provided the original work is properly cited, the use is non-commercial and no modifications or adaptations are made.

DOI: 10.1002/adma.202104878

A. D. Vito
Department of Electronic Engineering
University of Rome Tor Vergata
Via Cracovia, 50, Roma 00133, Italy

O. E. Glukhova
Laboratory of Biomedical Nanotechnology
I. M. Sechenov First Moscow State Medical University
Trubetskaya str. 8-2, Moscow 119991, Russia

P. M. Sheverdyeva, P. Moras
Institute of Structure of Matter (ISM-CNR)
SS 14 Km, Trieste 34149, Italy

I. Kaikov, I. Kiselev
Breitmeier Messtechnik GmbH
Englerstr. 27, 76275 Ettlingen, Germany

E. A. Kolesnikov
National University of Science & Technology (NUST) MISIS
Leninskiy Prospekt 4, Moscow 119049, Russia

a tailorable surface chemistry, low-noise metallic conductivity, mechanical flexibility, and easy processability at low costs.^[4,12,13] MXenes are typically synthesized from their corresponding ternary nanolaminated carbides and nitrides, such as MAX phases and MAX phase related materials, where A is an A-group element, followed by selective chemical etching protocols.^[14,15]

Among the diverse family of MXenes, $\text{Ti}_3\text{C}_2\text{T}_x$ is the most widely investigated material for various applications including gas-sensing.^[16] So far, $\text{Ti}_3\text{C}_2\text{T}_x$ has proved being sensitive to rather low concentrations of ketones (< to 50 ppb), alcohols (< to 100 ppb), and ammonia (< to 100 ppb) vapors at room temperature maturing from the impact of the analyte's physical adsorption changing the electronic properties in these low-noise materials.^[17–22] To further improve sensing properties of $\text{Ti}_3\text{C}_2\text{T}_x$ MXenes with respect to organic vapors, various approaches have been proposed including partial oxidizing at elevated temperatures up to 350 °C^[23] and composing hybrid hetero-composites.^[24] While most studies focus on $\text{Ti}_3\text{C}_2\text{T}_x$, investigations are not limited to Ti-based MXenes; other M-elements are currently successfully employed with extensive functional characterization.^[25] One of the most promising compounds is Mo_2CT_x which originates from a selective removal of Ga from its $\text{Mo}_2\text{Ga}_2\text{C}$ precursor^[26] in contrary to the more common etching of Al from corresponding Al-containing MAX phases. Mo_2CT_x is metallic as most MXenes^[26] and its hydrophilic nature already suggests this material for the hydrogen evolution reaction^[27] and as an potential anode material for energy storage applications.^[28] Recently, gas-sensing properties of Mo_2CT_x have been tested for aromatic hydrocarbons and volatile organic compounds (VOCs)^[29] set up in artificial background of N_2 in lieu of air. Moreover, along with the detection of VOCs the control of humidity in atmospheric air is essential for many processes and applications.^[30] In this sense, $\text{Ti}_3\text{C}_2\text{T}_x$ MXenes have been already widely examined for measuring the H_2O vapors and have demonstrated high humidity sensing capabilities^[31–36] with a rather fast response and a detection limit of 30 ppm.

Herein, we explore sensing properties of Mo_2CT_x MXenes toward humidity, as well as to other organic VOCs, alcohols, acetone, and ammonia in dry and wet air background from both experiments and theory. The designed sensors feature the superior sensitivity among pristine MXenes toward H_2O vapors with 10 ppm detection limit, which is the lowest value reported until now.

2. Results and Discussion

Mo_2CT_x MXenes have been successfully synthesized via HF chemical etching of Ga layers from $\text{Mo}_2\text{Ga}_2\text{C}$ parent layered ternary carbides, produced by pressure-less sintering following earlier protocols.^[37] Further delamination of the multilayer structure to single 2D sheets was achieved by intercalation with tetrabutylammonium hydroxide (TBAOH) as detailed in the Experimental Section. X-ray diffractometry (XRD) studies show that the $\text{Mo}_2\text{Ga}_2\text{C}$ precursor is almost single phase with a small amount of Mo_2C as a side phase (Figure 1a). The calculated lattice parameters (LPs) reveal rather large *c*-axis LP (18.0 Å) originating from two Ga layers stacking in-between Mo_2C layers

in the hexagonal crystal structure. Following the chemical etching, we received Mo_2CT_x MXenes whose XRD pattern is dominated by a sharp 002 reflex. The characteristic (002) peak shift of Mo_2CT_x toward lower angles as compared to $\text{Mo}_2\text{Ga}_2\text{C}$ indicates the larger spacing between the layers, which is also represented by an increased *c*-axis LP (20.5 Å) (Figure 1a).

The chemical etching of bulk $\text{Mo}_2\text{Ga}_2\text{C}$ precursor in HF results in the typical MXenes multilayered close-packed structure as revealed by scanning electron microscopy (SEM, Figure 1b). After intercalation of multilayer MXenes with TBAOH, transparent single or few-layered sheet-like structures with an average flake size of 500–800 nm and a smooth surface are visible in transmission electron microscopy (TEM) images (Figure 1c). Corresponding selected area electron diffraction (SAED) (Figure 1d) shows a high crystal quality of Mo_2CT_x flakes and a hexagonal structure inherited from the $\text{Mo}_2\text{Ga}_2\text{C}$ precursor; the measured *d* spacing is equal to 0.221 nm corresponding to the (0110) lattice plane. The height profile of Mo_2CT_x nanosheets recorded with atomic-force microscopy (AFM) (Figure 1e) indicates that their thickness is in the range of (4.7 ± 1.2) nm corresponding to the stack of two Mo_2CT_x layers further confirming the 2D nature of the synthesized material.

To investigate the nature of the surface terminations of the Mo_2CT_x MXenes as a result of chemical etching, high-resolution X-ray photoelectron spectroscopy (HR-XPS) analysis is performed (Figure 1f–h). The Mo-3d doublet with 3d_{5/2} components at 229.2 and 232.1 eV is shown in Figure 1f. The peak at 229.2 eV is attributed to Mo atoms bound to C and to surface termination groups, O– and OH–.^[26] The peak centered at 232.1 eV is assigned to Mo⁶⁺ oxidized species originating from air oxidation.^[26] The main C-1s core-level peaks (Figure 1g) appear at 283.2, 284.4, and 286.2 eV, which can be related to C–Mo bonds, organic C=C, and C–O contaminations, respectively.^[26] The O-1s spectrum shows three peaks at 530.0, 531.1, and 532.2 eV attributed in sequence to an MoO_3 oxide phase, C–Mo–O_x and C–Mo–OH oxygen bonds.^[26] Based on the obtained photoemission data and the proposed structural model of the MXene (Figure S1, Supporting Information), we calculate the ratio of Mo/C to be 1.89 ± 0.06 (Figures S2 and S3, Supporting Information). We note that this value is slightly smaller than the stoichiometric value of 2 derived from the chemical formula and it can be explained by overestimating the carbidic C content in the proposed structural model. The synthesized Mo_2CT_x MXenes are metallic as revealed by valence band spectra measured at $h\nu = 70$ eV and the non-negligible electron density at the Fermi level (Figure S4, Supporting Information).

High-resolution XPS spectra prove that the fabricated Mo_2CT_x MXene flakes are stable in air for at least 1 week (Figure S5, Supporting Information) when compared to as-prepared ones (Figure 1). This allows us the easy implementation of Mo_2CT_x MXenes into the gas-sensing device in order to perform the measurements in dry air environment. For this purpose, we use oxidized Si substrates equipped with multiple Pt strip electrodes with a length of $l = 4$ mm and gaps of $d = 50$ μm, which allows us to create an array of independent chemiresistive sensors on the single chip for simultaneous study in throughput experiments. The protocol scheme of such a prototype fabrication of chemiresistive multisensors is depicted in Figure 2.

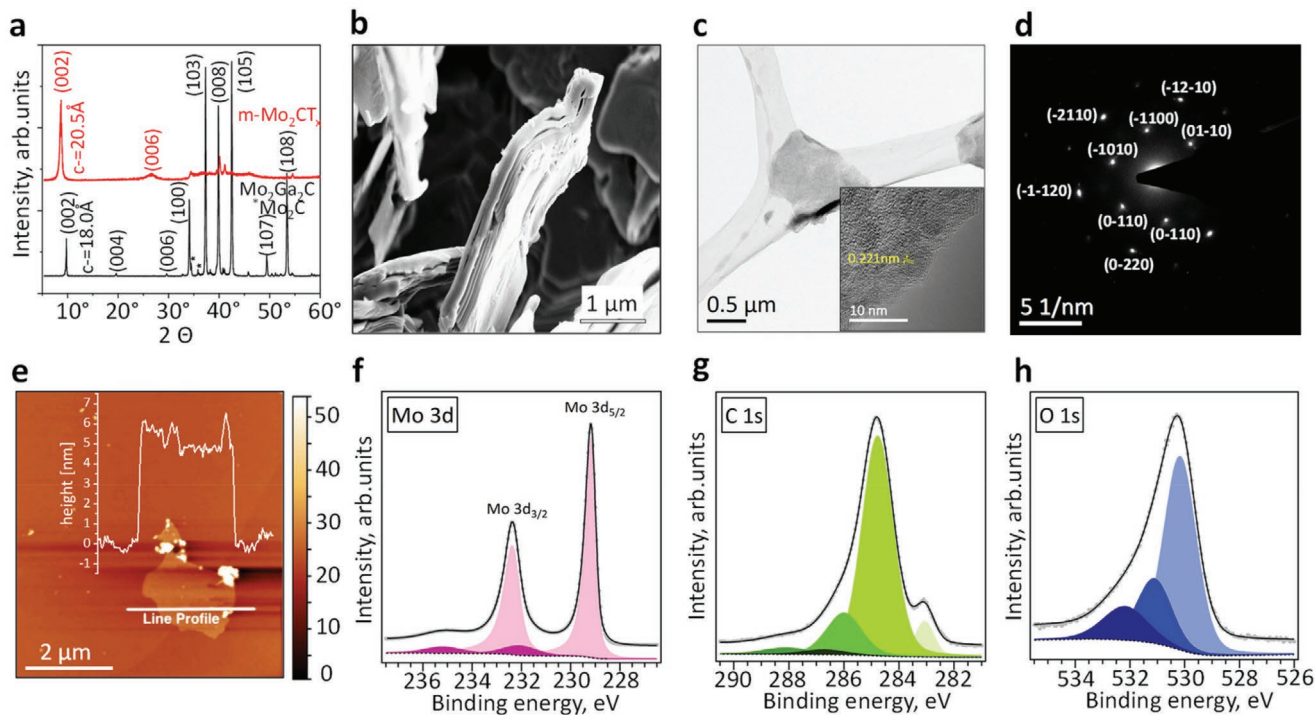


Figure 1. Structural and chemical characterization of Mo_2CT_x MXene. a) XRD patterns of $\text{Mo}_2\text{Ga}_2\text{C}$ nanolaminated carbide precursor (black) and Mo_2CT_x MXene multilayer (red). b) SEM image of a Mo_2CT_x MXene multilayer. c) TEM image of Mo_2CT_x MXene single flakes on lacey carbon grid, inset is a high-resolution image. d) The SAED pattern taken from the single Mo_2CT_x flake in c). e) AFM image and height profile over an exemplary Mo_2CT_x flake. f–h) High-resolution XPS spectra recorded from a Mo_2CT_x MXene layer at Mo-3d f), C-1s g), and O-1s h) energies.

As shown in the scheme in Figure 2a, the ternary nanolaminated $\text{Mo}_2\text{Ga}_2\text{C}$ precursor is chemically etched with HF to derive multilayered MXenes nanosheets consisting of a C atom network sandwiched between a pair of Mo sheets terminated

by surface functional groups (Figure 2b). The further delamination with TBAOH produces a stable suspension of delaminated Mo_2CT_x MXenes sheets. As detailed in the Experimental Section, these sheets are dispersed in distilled water under

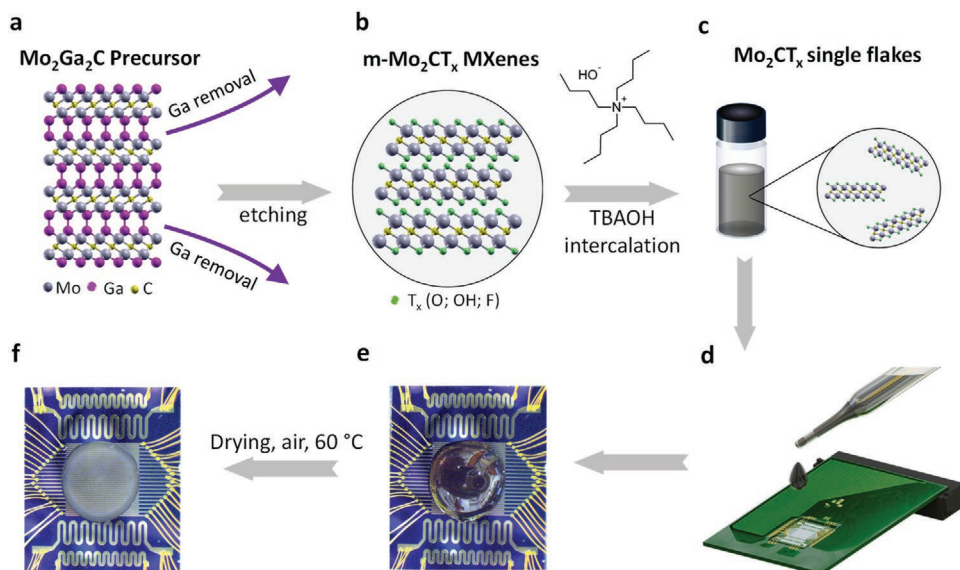


Figure 2. Schematic illustration of the fabrication procedure of Mo_2CT_x MXene-based multielectrode sensor chips. a) Crystal structure of $\text{Mo}_2\text{Ga}_2\text{C}$ MAX phase related material. b) Multilayer $m\text{-Mo}_2\text{CT}_x$ MXenes structure terminated by various T_x groups (green) inherited from chemical etchants. c) Delaminated MXene suspension containing Mo_2CT_x flakes. d) Drop-casting of Mo_2CT_x suspension over the sensor chip. e) Optical image of the chip with the as-deposited Mo_2CT_x suspension's drop on the surface. f) Optical image of the final sensor after drying.

ultrasonic treatment (Figure 2c). Finally, the as-prepared aqueous Mo_2CT_x suspension has been drop-casted over the chip to cover the electrode area (Figure 2d) with subsequent drying at 60 °C in air. The optical images of the chip coated just with the suspension drop and the final sensor array are shown in Figure 2e,f; and Video, Supporting Information shows the drying of droplet on the chip.

The fabricated chips have been thoroughly inspected by electron microscopy in par with energy-dispersive X-ray spectroscopy (EDX) analysis. Figure S6a (Supporting Information) gives an overview of the whole chip. In accordance with optical images, it shows the Mo_2CT_x layer homogeneously covers the multiple electrodes within the circular shaped droplet with 4.4 ± 0.1 mm diameter. The covered area is highlighted in dark yellow in Figure S6a (Supporting Information). To identify the elemental composition of the layer, we employed EDX mapping at the circle rim. As shown in Figure S6b (Supporting Information), we identify the presence of Mo and C in the layer together with O, Si, and Pt originating from the substrate and the electrodes. Still, the Mo_2CT_x layer is thin enough to allow the transmission of soft X-rays from the substrate. SEM images at higher magnification displayed in Figure S6c (Supporting Information) further exhibit the smoothness of the layer which consists mostly of nm-scaled flakes with some inclusions of sub- μm - and μm -sized agglomerates, which seems to remain after the ultrasound treatment. The layer covers both the substrate at the interelectrode gap and the electrodes themselves. However, the Mo_2CT_x flakes tend to be confined both between metal electrodes as a layer whose conductivity is being measured and on top of electrodes. These SEM observations are further supported by profilometer measurements; see Figure S7 (Supporting Information). We have analyzed the lateral length λ of the Mo_2CT_x flakes from several SEM images of the layer surface taken at different locations on the chip. It follows a Gaussian distribution with the peak position at about 185 nm. Most flakes have a size between 75 and 300 nm with some rare agglomerates. It is worth noting that the micrometer-sized flakes, though being at a minor quantity, might shunt smaller flakes. This leads to a variation of the observed local resistance values measured via multiple electrodes. The typical EDX spectrum of Mo_2CT_x flakes is pictured in Figure S6d (Supporting Information). It further qualitatively supports the presence of Mo, C, O, and Si elements, and indicates the atomic ratio between [Mo] and [C] to match the chemical formula in a full coincidence with the photoemission data (Figures S2 and S3, Supporting Information,) taken at as-prepared single flakes.

To estimate the thickness of the Mo_2CT_x layer deposited over the chip we have applied stylus profilometry across the electrodes of the chip before and after the casting. The estimation of the profile along the electrodes has been found too tricky because of the rather narrow interelectrode distance, of less than 50 μm , and the trapezoid shape of electrodes which could contribute to the measurements at μm -shifts of the stylus. Therefore, the layer thickness, h , has been taken as the difference between cross-electrode profiles of the pristine and the coated chip. To further verify this estimate, the profile scans have also been taken in uncoated areas of the chip (Figure S6e, Supporting Information) serving as a reference. We have found that the layer is distributed rather uniformly with the thickness

ranging from about 92 to 527 nm with the largest thickness close to the layer edges with a narrow rim (clearly seen in Figure S6b at about 15 μm). This layer inhomogeneity seems to be driven by surface tension of the water-based suspension which forces the light particles of the dropped Mo_2CT_x flakes to move to the drop interface and remain there after drying. This intrinsic variation of the layer thickness over the chip allows us, i) the simultaneous test of the Mo_2CT_x layer functional properties according to throughput protocols^[38] and ii) to employ multiple channels to advance the gas-selectivity performance of the chip as further discussed below. Accounting to the flake's height to be up to 5 nm (Figure 1), the deposited layer is composed of multistacked of 30–210 flakes. The given layer thickness has been selected to provide both a percolation among the MXene flakes and a good gas access to the material from the environment.

The gas-sensing properties of the Mo_2CT_x layer have been studied in a flow-mode setup where test analytes (water, alcohols, ammonia, and acetone) have been supplied by bubbling of air through the corresponding liquids. As detailed in Figure 3a, we have arranged a proper delivery of the analytes to the chip at various concentrations in the 10^1 – 10^4 ppm range, driven by high-precision mass-flow controllers mixing in dried and filtered lab air, which is also taken as a reference. The resistance of the local Mo_2CT_x layer segment confined between each couple of coplanar electrodes configured at the chip has been read out with a low-noise amplifier and multiplexing cards. The latter served as a sequential switch for bias voltage of 1 V, applied to neighboring electrodes across the total set in the array. To verify the analyte exposure, we have supplemented the gas output by a low-cost commercial humidity sensor of capacitance type as detailed in the Experimental Section which allowed us to directly compare the performance of the Mo_2CT_x sensor under study. The measurements were taken primarily at room temperature, varying in the range of 28–35 °C, while some experiments have been taken at elevated temperatures up to 100 °C using the built-in heater meanders regulated by a PC-driven proportional-integral-derivative (PID) regulator.

The exposure of the Mo_2CT_x layer to humidity results in a pronounced increase of the material's resistance. As shown in Figure 3c for three exemplary sensors of the array, distinguished by different resistance values, the resistance follows the H_2O content in the flowing air in a reproducible and reversible manner in line with a conventional chemiresistor's behavior. Higher concentrations result in larger increase of resistance observed in transient $R(t)$ curves. This chemiresistive signal is stable and reproducible as shown, for example, in Figure 3c for a few days of continuous operation under multiple repetitions of H_2O exposures. Importantly, the sensing properties are preserved even when the sensor chip is stored for 6 months in ambient air (Figure S8, Supporting Information) although the sensor resistance matured from partial oxidation of the MXenes.

The same behavior has been observed in relation to other analytes under this study (alcohols, acetone, and ammonia) but at lower magnitudes (Figure S9, Supporting Information). In contrast to the capacitive sensor, the developed Mo_2CT_x sensors yield a rather high and distinguished chemiresistive signal versus 10–30 ppm H_2O , while the commercial capacitive sensor

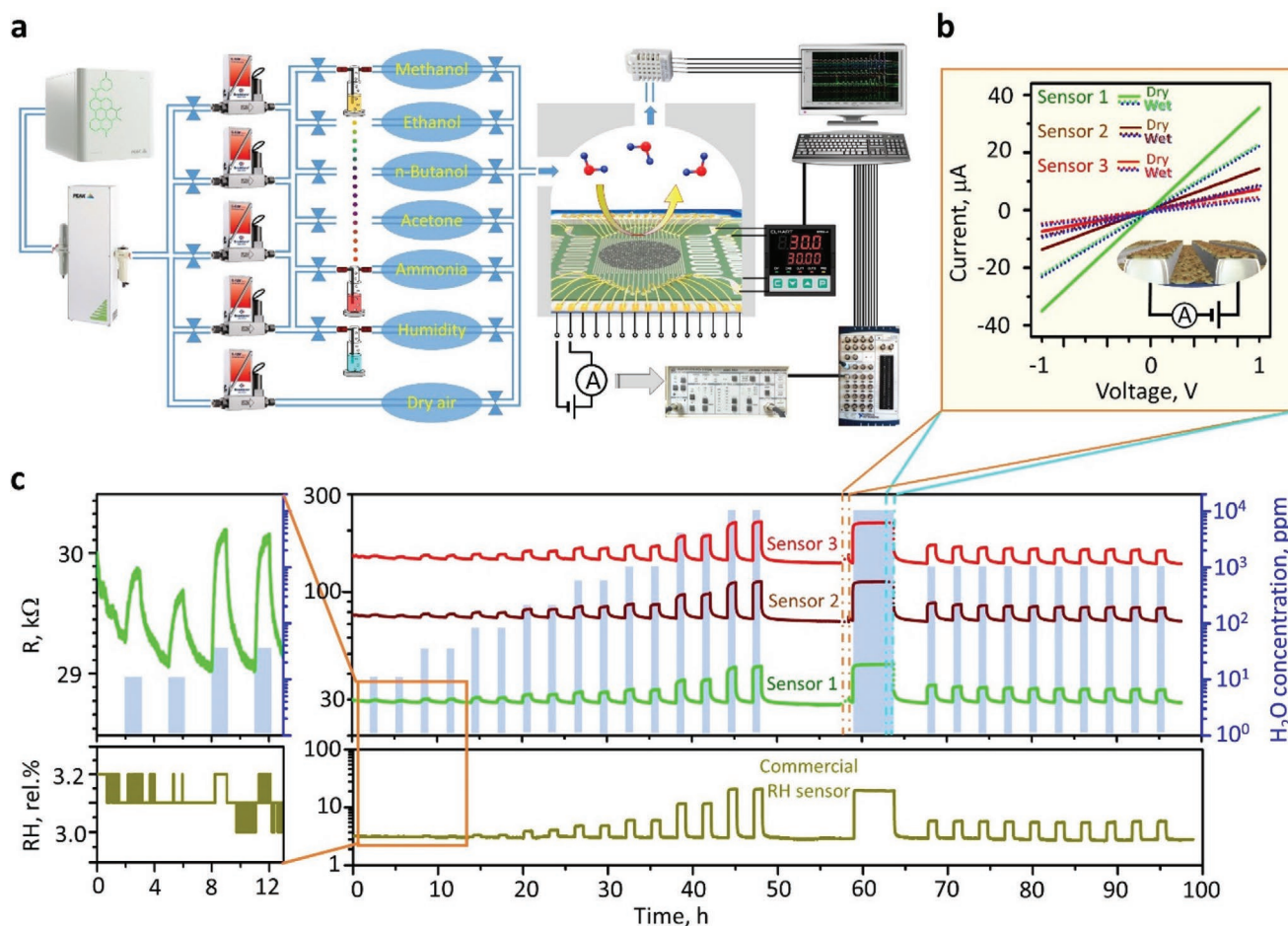


Figure 3. Humidity-sensing of the multisensor based on a Mo_2CT_x layer. a) The measuring setup composed of, i) analyte probe, bubblers, delivery to the sensor through high precision flow controllers, and ii) signal-reading electronic scheme equipped with multiplexing cards. b) I - V curves measured under dry and high humidity, $\approx 10^4$ ppm, c) long-term $R(t)$ transients measured under multiple exposures of the chip to H_2O vapors of various concentrations at room temperature when compared to a commercial capacitive sensor calibrated to show the humidity content, RH, in rel%. The light-blue bars show the chip's exposure to humidity at concentrations given in the right ordinate axis.

fails, in fact, to show humidity changes (Figure 3c, inset). The lower sensitivity of the commercial sensor also holds for comparative studies of alcohols, ammonia, and acetone in full agreement with other 2D materials including graphene.^[39] To ensure the origin of the resistance, we have checked I - V curves recorded in dry air and humid-enriched atmosphere with $\approx 10^4$ ppm H_2O concentration. Figure 3b depicts the expected linear Ohmic behavior under both environmental conditions allowing to exclude significant potential barriers at the Mo_2CT_x /electrode interface. This seems to originate from the proximity of the work functions of Mo_2CT_x , 4.22 ± 0.15 eV (Figure S10, Supporting Information), and Pt (5.15 eV).^[40]

To quantify the resistivity of the Mo_2CT_x layer, we have matched the profilometry measurements taking into account the layer geometry and resistances recorded from I - V curves. The estimated resistivity values of the Mo_2CT_x layer are $1.18 \pm 0.36 \Omega \text{ m}$ in dry air and $1.90 \pm 0.36 \Omega \text{ m}$ in humid-enriched air (Figure S11, Supporting Information), which is similar to a $9 \mu\text{m}$ thick Mo_2C layer reported before.^[26] Such resistivity is still six orders of magnitude higher than ones known for a single Mo_2C crystal^[41] and for few-nm spin-coated $\text{Ti}_3\text{C}_2\text{T}_x$ MXenes.^[36]

This clear difference seems to appear primarily due to the huge number of Mo_2CT_x layers and electrons pass between electrodes. The charge carrier transport is limited by the interflake boundaries. This feature is further clarified when applying ac electric fields as discussed below.

The relative chemiresistive signal change has been determined from the resistance, R , with respect to the one recorded in dry air, R_{air} , as

$$S = \frac{R - R_{\text{air}}}{R_{\text{air}}} \cdot 100\% \quad (1)$$

We plot this signal in dependence on the analyte's concentration C in Figure 4a on a log-log scale to demonstrate the high flexibility of the new sensor over 3 decades. As one can see, the signal to the analytes obeys, in general, the $S \sim C^n$ behavior in accordance with the Freundlich isotherm. The exponent, n , varies between 0.34 and 0.51 for different analytes (Table S1, Supporting Information), and is equal to 0.47 ± 0.02 specifically for humidity vapors. We have limited the low concentrations of other analytes down to 500 ppm because of the sensor's lower sensitivity.

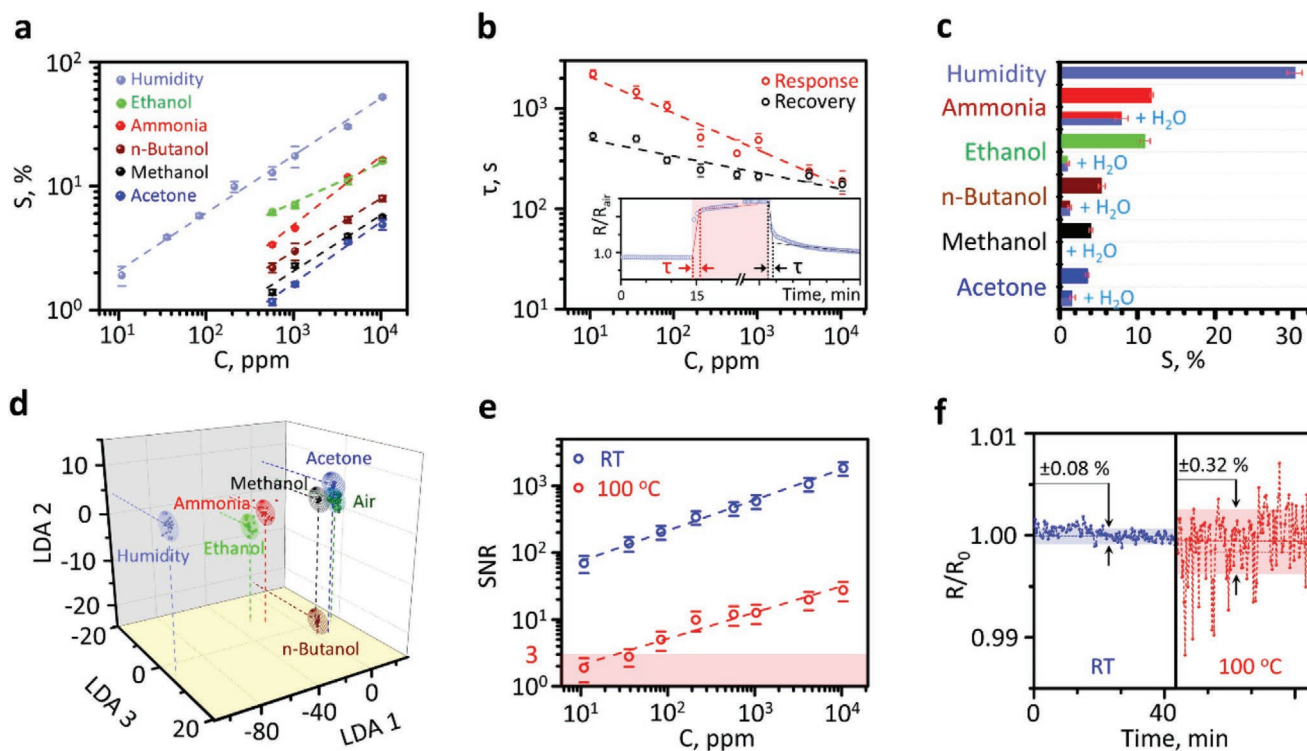


Figure 4. Performance parameters of the Mo_2CT_x -based multisensor prototype under dc electrical bias. a) The chemiresistive response to H_2O and other analytes versus their concentration. b) Response/recovery time, τ , versus H_2O concentration; inset is the method to estimate the characteristic times using $R(t)$ transient. c) The comparison of response to various analytes at concentration of $C = 4000$ ppm. d) LDA processing of multisensor signal recorded from the sensor array, 3D cross section of primary 1–3 LDA components in the total 6D LDA space; ellipses confine the LDA space around gravity centers related to analytes, all at $\approx 10^4$ ppm concentration, built by a Gaussian distribution with confidence probability of 0.75. e) Signal-to-noise ratio, SNR, versus the H_2O concentration measured at room temperature (RT) and at 100°C . f) The typical resistive noise of an exemplary sensor measured at RT and 100°C , the values show standard deviations relative to median R_0 . The data at a), b), c), e) are supplied with error bars of standard deviations.

The characteristic times of the Mo_2CT_x layer's response/recovery to H_2O as the major-influenced analyte depend on its concentration. Figure 4b displays the response and recovery times to vary from ≈ 1000 to 2000 s at 10 ppm to ≈ 200 s at $10\,000$ ppm, which is enough for most applications related to humidity monitoring;^[42] the method for estimating these parameters as a component of the rapid $R(t)$ change is shown in the inset of Figure 4b. We believe that the characteristic times of the Mo_2CT_x sensor primarily relies on both, the analyte's delivery in the flow-driven experimental setup and, possibly, a diffusion of gas molecules into the film. Still, the proper estimate of these parameters should be further carried out in a vacuum chamber which ensures fast-changing atmospheres.

As evidenced from the observed data of Figure 4a, the response to H_2O vapors is apparently higher than to other analytes. Moreover, if the Mo_2CT_x sensor is exposed to humid air at a rather high concentration of 10^4 ppm (or about 25% rel. humidity), the response to the other analytes is suppressed. The same effect of suppressing the gas response to other analytes at humid atmospheres was observed for alkalinized V_2CT_x MXenes, however at higher humidity values ($>60\%$ RH) as compared to our finding ($>25\%$ RH).^[43]

We summarize this finding in Figure 4c showing comparatively the chemiresistive response of the sensor to analytes of

4000 ppm in dry and humid-enriched 10^4 ppm atmosphere. While the sensor response to NH_3 is reduced from 12% to 8%, the Mo_2CT_x flakes become almost insensitive to organic vapor analytes. For instance, the signal for methanol disappears under these conditions in humid environment. This could be due to the competition between preferential formation of hydrogen bonds by water adsorption on MXene' surfaces^[44] and alcohols/water interaction possibly result in a weakening of the formed hydrogen bond network.^[45] This indicates that humidity has a strong and rather selective impact on the Mo_2CT_x flake surface and the chemiresistive effect in this material that gives further opportunities to separate analytes.

Nevertheless, the Mo_2CT_x sensor has no absolute selectivity to the humidity vapors similar to most other gas sensors.^[46] Therefore, we further study the selectivity by the multisensor vector signal collected from the all Mo_2CT_x sensors of the chip and processed it as an analyte-specific pattern according to the E-nose concept.^[47] For this purpose, the resistance data recorded at the quasistationary conditions under each analyte exposure have been collected to a database and processed by a linear discriminant analysis (LDA) algorithm^[48] with custom-developed software as detailed in the Experimental Section. Obviously, we considered the most interesting case to discriminate the analytes of 4000 ppm in a mixture with dry air accounting for the

almost negligible response of the Mo_2CT_x sensor to analytes in humid-enriched air. The LDA technique transfers the multidimensional vector signal of the multisensor array into an optimized artificial coordinate system. The specific features related to various inputs (analytes in this case) are maximized related to the fluctuations observed under the same analyte exposure considering the ratio of $\frac{\text{inter-class variation}}{\text{in-class variation}}$. This is possibly the most powerful method to discriminate these patterns with a clear illustrative understanding of the received data in comparison to the alternative of artificial neural networks.^[49] The dimensionality of such LDA space is defined by a number of distinguished inputs N , which is equal to 7 in our case taking into account the input of 6 analytes and 1 for dry air as the reference background. In the study, we have plotted the 3D projection of three primary LDA components of 6D LDA space in Figure 4d. The points represent the multisensor array resistances at a specific atmosphere. The LDA analysis clusters these points into corresponding analyte-related groups, which we surround with frame ellipses around the gravity centers of the clusters supposing a scattering behavior of the data within each class following a Gaussian distribution. As an example, we took the 0.75 confidence probability to border the ellipses which is enough to see the discrimination of analyte-related clusters. Notably, the H_2O -related ellipse exhibits to be the most distanced one from the dry air-one at ≈ 127 units of the LDA coordinate system, and other analytes as well; the complete dataset of Euclidian distances between air and other analytes are given in Table S2 (Supporting Information). Thus, the humidity effect on the Mo_2CT_x layer resistance could be further selectively distinguished with a high degree by taking the multisensor signal of the chip array where the variation of gas-sensing properties in the array has an intrinsically stochastic nature. Still, we should note that methanol-related cluster of vector signals is distinguished from ethanol- and butanol- signals that has a direct practical interest.^[50] Further advancement of such a recognition could be approached by a gradual functionalization of the layer surface with foreign atoms or intrinsic defects.^[51]

One option to advance the sensitivity of the Mo_2CT_x sensor is its operation temperature. We have heated the layer to 100 °C by utilizing built-in meander heaters located on the chip. The higher temperature could facilitate the appearance of the oxide phase on the MXenes surface^[23] which was, however, not in the scope of this study. The heating resulted in a significant drop of the chemiresistive signal as shown in Figure 4e. The signal-to-noise ratio (SNR) is plotted, which is frequently considered as an appropriate parameter to compare sensors, as a function of H_2O concentration C . At room temperature the SNR is 70 ± 20 at 10 ppm of humidity that is 300% improved as compared to other sensors^[52] and highlighted in red in Figure 4e. At the same time, the SNR recorded at 100 °C is equal to 2 ± 1 , i.e., the sensor signal is comparable to the resistive noise. In general, the calculated SNR at 100 °C is 2–3 orders of magnitude lower than the one at room temperature and the detection limit is observed at ≈ 25 ppm of H_2O concentration. Such a degrading sensor performance seems to be primarily matured from the rising resistance noise amplitude due to the thermal excitation of phonon oscillations in the Mo_2CT_x flakes.^[53] Indeed, Figure 4f shows the noise levels of the exemplary

Table 1. Summary of the experimental reports on H_2O vapors-sensing performance of MXene-based layers.

Material	Humidity sensing features	Ref.
Alkalinized $\text{Ti}_3\text{C}_2\text{T}_x$	11–98% RH range. Repeatability at 98% RH, 1 s response, 201 s recovery	[31]
$\text{Ti}_3\text{C}_2\text{T}_x/\text{poly}$ (diallyldimethylammonium chloride)	10–70% RH. 110 ms response, 220 ms recovery. Monitoring of human breathing.	[32]
Ti_3C_2	0.1–95% RH range. LOD is 0.1% RH (30 ppm H_2O)	[54]
TiO_2 nanowires on Ti_3C_2 MXene	7–97% RH range. Sensitivity: ≈ 280 pF/% RH in 7–33% RH.	[55]
K^+ and Mg^{2+} ion-intercalated Ti_3C_2 MXene	5–90% RH range. LOD is $\approx 0.8\%$ RH.	[56]
$\text{Ti}_3\text{C}_2\text{T}_x$ MXene Fabric	20–80% RH range.	[57]
$\text{Ti}_3\text{C}_2/\text{Ag}$ composites	8–85% RH range. 5 s response, 80 s recovery.	[58]

Mo_2CT_x sensor recorded both at room temperature and 100 °C. Figure S12 (Supporting Information) yields infrared images of the chip taken under these conditions with a high resolution of 21 μm . As one can see, the relative amplitude of the resistance noise is very low at room temperature and does not exceed 0.08% in accordance with other studies on MXene-based sensors,^[19] while it is enhanced by four times, up to 0.32%, under heating. Thus, these data further promote the Mo_2CT_x sensor as promising one for operating at room-temperature conditions to meet applications where lower energy consumption is required.

To compare the observed H_2O -sensing performance of this sensor prototype, we have reviewed MXene recent studies in Table 1 and plotted the comparative diagram of gas sensitivity coefficient, calculated as the ratio of S/C ,^[23] in Figure 5; this parameter is suitable to properly compare the diverse data published in the literature. As one can see, the overall performance of the studied Mo_2CT_x sensor versus humidity exceeds the data reported for other MXene-based sensors. Moreover, Mo_2CT_x sensor is able to detect humidity with a sensitivity down to 10 ppm at room temperature, which is the lowest value for H_2O vapors detection among MXenes. Additionally, the presented Mo_2CT_x sensor demonstrates enhanced performance (RH 25%) as compared to recently employed MoS_2 and VS_2 2D materials having a low RH range with a sensitivity of 30–150%.^[59]

Impedance spectroscopy is a powerful method to excite charge carriers in a material by ac electric fields and allows to formalize the electric processes by creating equivalent circuits.^[60] Here we have applied the ac electric biases of 0.1 and 1 V in the frequency range of 10^{-2} – 10^6 Hz via the same couples of electrodes that were employed for dc resistive measurements before. The impedance, Z , of the Mo_2CT_x sensors as function of frequency, f , is drawn in Figure 6a for dry air and humidity-enriched, 10^4 ppm concentration, air environments. First, we have not observed any significant differences in the $Z(f)$ curves recorded at ac electric fields, amplitudes of $E = 2 \times 10^3$ and 20×10^3 V m^{-1} , which indicates the free carrier transport is similar for both biases. Second, the ac measurements further support the increasing resistivity of the Mo_2CT_x layer in humid

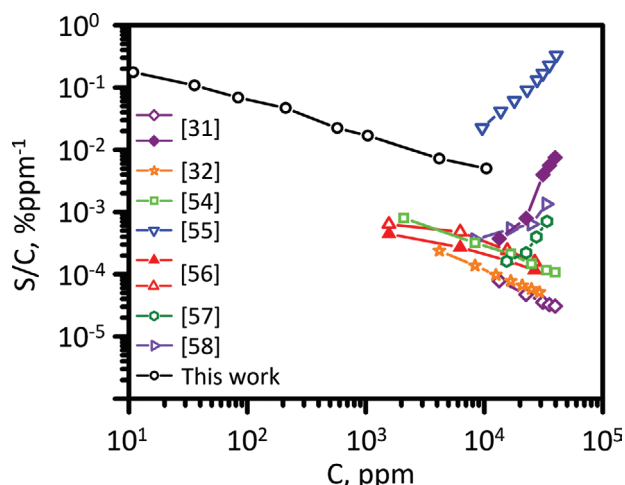


Figure 5. The humidity-sensing performance of the Mo_2CT_x -based sensor prototype in comparison to other data reported in MXene-based structures. The comparison is given via a gas-sensitivity coefficient defined as the ratio of sensor signal S , in percent, to H_2O concentration C , in ppm.

environment. The $Z(f)$ curve measured in H_2O reaches higher Z values than the one measured under dry conditions when the ac frequency is below 10^5 Hz. The Z values recorded at a low-frequency range down to 10^{-2} Hz correspond quite well to the resistance values observed in the dc measurements.

The characteristic frequency when capacitive effects start dominating the impedance is $\approx 4 \times 10^4$ Hz. We have fitted the observed $Z(f)$ curves by an equivalent electric circuit consisting of three RC elements in series as drawn in the insert of

Figure 6a. The approximation was quite good with errors not exceeding 6% for the R components and 15% for the C components, both to characterize the 3rd RC-element (Figure S13, Supporting Information). The resistance values are found in the $\text{k}\Omega$ range (Figure S13, Supporting Information) in agreement to dc experiments. At the same time, capacitances are calculated to be at $\approx 10^{-11}$ F (C_1), $\approx 10^{-10}$ F (C_2), and $\approx 10^{-8}$ F (C_3) which allow us to assign^[61] the corresponding RC-elements as characterizing the Mo_2CT_x flakes themselves, flake-to-flake and flake-to-electrode interfaces. The related Nyquist plots are shown in Figure 6b for dry and humid air. We have plotted the characteristic semicircles based on the RC elements to quantify the corresponding frequency ranges. As one can see, the humidity enhances not only the real part of impedance, Z' , in agreement with dc measurements, but also reduces slightly an imaginary part of impedance, Z'' , defined by a capacitance.

The $Z(f)$ curves allow to extract the potential barriers when considering the conductivity, σ , of a multiflake morphology with frequency as a power law according to Jonscher as^[62]

$$\sigma_{ac}(f) = \sigma_{dc} + Af^s \quad (2)$$

where $\sigma_{ac}(f)$ is evaluated accounting for the layer's geometry as $\sigma_{ac}(f) = d(Zhl)^{-1}$, σ_{dc} is the dc conductivity, A and s are coefficients which characterize the material at the given temperature. In particular, the empirical value of s indicates the kind of electronic transport to be a translational one when $s < 1$ or a localized one when $s > 1$.^[63]

This s parameter can be empirically extracted from $\sigma_{ac}(f)$ as $s = d(\ln(\sigma_{ac} - \sigma_{dc}))/d(\ln f)$. We have plotted s as a function of

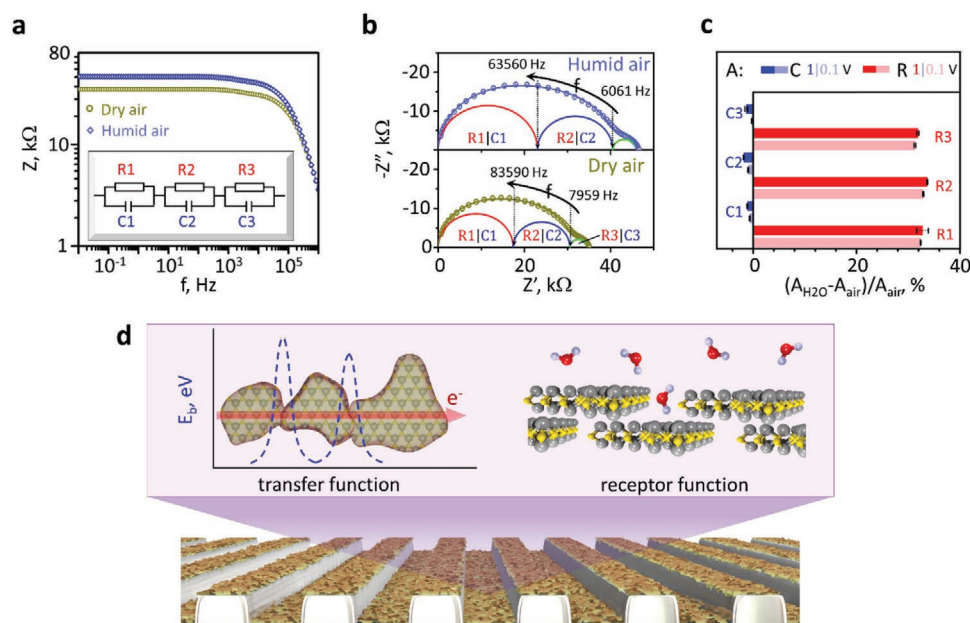


Figure 6. Performance parameters of the Mo_2CT_x -based sensor prototype under ac electrical bias and a concept to explain the chemiresistive effect by impedance spectroscopy. a) The dependence of impedance, Z , of an exemplary sensor versus ac frequency, f , measured in dry air and humid-enriched air, $\approx 10^4$ ppm concentration; inset is the equivalency electrical circuit. b) The typical Nyquist plot characterizing an exemplary sensor when measured in dry air and humid-enriched air fitted by the electrical circuit a), the amplitude of the ac electric bias is 0.1 V. c) The relative change of equivalency electrical circuit's parameters, resistance R and capacitance C , upon exposing to humidity at 0.1 and 1 V bias voltage. d) The general concept of the effect measured employing multiple chip electrodes: the transfer function is driven by barrier-controlled electron transport, the receptor function is governed by analyte's adsorption over the crystal surface.

frequency (Figure S14, Supporting Information). It is found that the s value is less than 1 that supports the translational mechanism of carrier's transport which accounts for the potential barriers. Still, the varied magnitude of $s(f)$ reflects rather complex contributions which should be clarified in the following studies. Knowing s , we may implement a model of correlated barrier hopping^[64] in order to estimate an effective barrier height E_b for electronic transport in the material as

$$s = 1 - \frac{6kT}{E_b} \quad (3)$$

where k is Boltzmann's constant and T is the operating temperature, ≈ 300 K in our case. The calculated E_b values have been plotted as function of frequency (Figure S14, Supporting Information). In the part of this curve which corresponds to the second RC-element the calculated magnitude of E_b is below 0.17 eV, while this is below 0.2 eV in the total frequency range. Notably, the appearance of humidity does not significantly change the barrier's height in the Mo_2CT_x layer, which indicates that the observed resistance change occurs primarily due to processes at the flakes themselves. The potential barriers at the flake-to-flake interfaces exceed the energies which electrons could acquire under the applied dc electric fields. Indeed, assuming electron's ballistic propagation through the single Mo_2CT_x flake of mean size λ , it acquires energy of $\phi = E\lambda$ (in eVs) equal to $0.4\text{--}3.7 \times 10^{-3}$ eV which is still much lower when compared to E_b . Therefore, the dc I - V curves are Ohmic.

Most interesting here is the estimation of the electric parameters when the sensor is exposed to humidity. Figure 6c displays the relative change of both R and C in percent similar to the dc chemiresistive response (1), where A denotes the R1-R3 or C1-C3 components of the equivalency circuit.

As one can see in Figure 6c, all resistance values increase up to 32% when Mo_2CT_x is exposed to H_2O vapors which is in quantitative agreement to the dc behavior (Figure 4c), while the capacitance goes in an opposite direction. The relative variation of capacitance induced by H_2O ($\approx 3\%$) is almost one order lower than the noted one of resistance.

With these experimental observations, we propose that the chemiresistive effect in the Mo_2CT_x layer is driven by a barrier-governed transport of electrons which defines the sensor's transfer function as depicted in Figure 6c. Further experiments with this material, especially in a single flake arrangement, could elucidate the contribution of interflake junctions to H_2O and other VOCs adsorption and overall gas sensing. However, the interaction of the MXene's surface with analytes from a gaseous phase governs still the sensor's receptor function. Here, it is worth noting that we cannot exclude a diffusion of analyte molecules within the poly-flake layer as suggested earlier for the poly-flake rGO films^[49] to explain the more effective access of humidity molecules to the flake's surface when compared to, for instance, alcohols. This mechanism could further contribute to the receptor function of the Mo_2CT_x chemiresistor.

The efficiency of interaction between gaseous analytes and the MXene surface could be approached by ab initio calculations under the density functional theory (DFT).

With this purpose, we have considered the Mo_2C crystal as a basic platform to estimate the fundamental effect of analytes on the free charge carriers in the crystal and its related electrical

parameter variations. The unit cell of Mo_2C crystalizes in the $\bar{6}m2$ point group containing 1 C atom and 2 Mo atoms. To simulate the MXene's sheet exposure to the adsorption of various analytes, we have constructed a supercell by the translation of 25 unit cells in Y and Z directions (Figure 7a). The details of the algorithm are given in the Experimental Section. The electrical conductivity of the Mo_2C crystal supercell has been calculated in the Z direction at pristine and analyte-disturbed configurations. We have chosen the case of a single molecule's adsorption to study primarily its qualitative effect on the material's resistance. Figure 7b yields a fragment of the Mo_2C supercell mapping the electron density distribution over the atoms calculated within the framework of Mulliken's formalism when the analyte molecules of interest approach the surface. Primarily, we evaluated the MXene covered with a molecule as a first approximation. This is obviously not the maximum H_2O concentration over the Mo_2C supercell but even a single H_2O molecule leads to a rather perceptible redistribution of the electron density at the surface (1, Figure 7b). The water molecule yields 0.042e to the supercell in framework of Mulliken's formalism. As one can see from the charge mapping, the Mo atoms located just below the H_2O molecule take a noticeable negative charge, highlighted in blue, $\approx 0.023e$. A similar situation is observed for all the analyte molecules under study (3–6, Figure 7b) except for NH_3 (2, Figure 7b). It should be noted that we analyze the adsorption of single molecules for other analytes, too, i.e., the model is applicable to the lowest analyte concentration. The NH_3 molecule takes charge of 0.024e from Mo_2C MXene (Table 2). Figure 7b (2) shows that ammonia molecule does not excite a strong charge redistribution over the supercell's surface, to be in the range of $-0.16e - +0.054e$. At the same time, the alcohol and acetone molecules induce a charge transfer toward the surface. In Figure 7b (3–6), we can see the characteristic areas of Mo_2C surface containing an excessive charge just under the analyte molecules. The amount of charge transferred to the surface strongly follows the number of atoms in the analyte. It is worth noting that the amount of transferred charge in case of "heavy" analytes as butanol and acetone is almost the same as for water. This is explained by the stronger binding energy between H_2O and the Mo_2C supercell (Table 2) which is calculated as the difference between the energy of surface/analyte system and the sum of analyte and surface energies prior their interaction. We may note that the adsorbed H_2O molecule has the strongest binding energy equal to 0.125 eV among all the tested analytes, which exhibit energies in the range of 0.03–0.06 eV. It further proves the humidity's dominancy and stronger influence on the Mo_2C . This value correlates well with similar data on MoSe_2 ,^[65] MoS_2 ,^[66] as well as on metal^[67] and FeO ^[68] surfaces. Notably, such binding energies still satisfy the conditions for a reversible chemiresistive effect when the molecules could desorb from the Mo_2C surface at room temperature. At the same time, these adsorption processes yield a shift of the Fermi level (Table 2) with the corresponding reduction of electronic states which results in reduced resistance values for all the analytes under study.

Figure 7c plots the density of electronic states (DoS) as function of energy for the Mo_2C supercell disturbed by the various studied adsorbed analytes. The DoS maximums are observed at the Fermi level, indicated at Table 2, that justifies a high

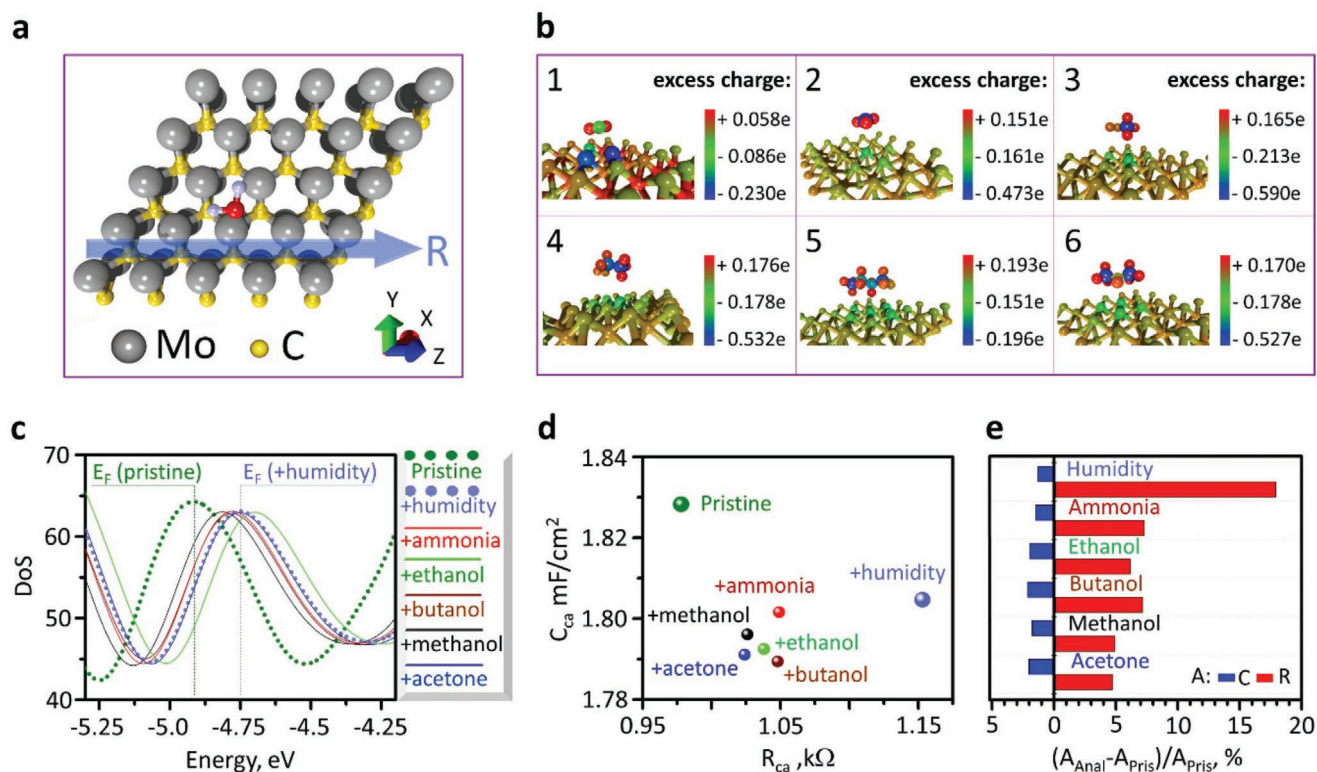


Figure 7. Receptor function of chemiresistive effect in 2D Mo_2CT_x flakes. a) The Mo_2C supercell taken for the DFT studies, the direction of resistance's calculation over the supercell with adsorbed H_2O molecule as an example. b) The energy-colored state of the supercell and excess charge upon single-molecule analyte's adsorption of 1) humidity, 2) ammonia, 3) methanol, 4) ethanol, 5) butanol, 6) acetone. c) DoS distribution calculated by DFT under adsorption of various analyte molecules over Mo_2C supercell. d) The c-a resistance, R_{ca} , and quantum capacitance, C_{ca} , values of the Mo_2C supercell when exposed to various single-molecule analytes. e) The c-a relative variation of resistance R_{ca} and capacitance C_{ca} upon the adsorption of various single-molecule analytes (A_{Anal}) versus ones characterizing the pristine surface (A_{Prist}).

conductivity of the structure regardless of the kind of analytes. It is clear that there is a tendency for analytes to shift the Fermi level to zero value. The highest DoS is observed for the pristine surface while all analytes reduce the DoS.

We have approached the supercell's resistance within the Landauer–Büttiker formalism which allows us estimating the current through the supercell as a transmission function T . To calculate the function, the semi-infinite source–drain electrodes have been considered along the Z-axis direction of the supercell (Figure 7a). In the case of 2D structures, the T function depends on two variables, the electron energy, E , and the wavenumber k_y ; the latter defines the electron's momentum.

It is worth noting that we exclusively consider here the y component k_y of the wavenumber since k_z has been taken into account during the construction of the semi-infinite electrodes. Furthermore, the $T(E)$ function is calculated by averaging over all the k_y values. The transmission function is calculated by

solving the nonstationary Schrödinger equation applying the nonequilibrium Green–Keldysh functions and the Lippmann–Schwinger equation. The latter allows us quantifying the wave function for a perturbed system in terms of the wave function of the unperturbed system and the corresponding Green's operator. As the result, we have calculated the conductivity and quantum capacitance, see Section S8 in the Supporting Information for details.

Figure 7d yields a plot of the calculated resistance and quantum capacitance of the Mo_2C supercell under adsorption of various analyte molecules. The resistance of the Mo_2C supercell ranges from $R = 0.97$ k Ω characterizing the pristine state to higher values under analyte's adsorption reaching $R = 1.16$ k Ω in case of humidity. All other analytes result in intermediate resistances. The diagram gives the capacitance values at $V = 0$ V in specific units of mF cm^{-2} . As one can see, the pristine Mo_2C supercell has $C_q = 1.8283$ mF cm^{-2} which is

Table 2. The energetic and electronic characteristics of the Mo_2C supercell under interaction with analyte molecules.

Analyte	No (pristine surface)	Humidity	Ammonia	Methanol	Ethanol	Butanol	Acetone
Binding energy, eV	—	−0.125	−0.064	−0.046	−0.042	−0.033	−0.042
Excess charge, e	—	−0.042	0.024	−0.019	−0.010	−0.046	−0.045
Fermi level, eV	−4.916	−4.751	−4.778	−4.814	−4.700	−4.779	−4.750

approximately one order higher than one recently estimated for 2D MoS₂ layer.^[69] When analytes appear on the Mo₂C surface, the capacitance reduces for all studied molecules including H₂O. This trend is reasoned by both the DoS intensity reduction and the increase of the mass of the supercell with the adsorbed analyte.

To compare DFT-results with experimental data on chemiresistive effect, we have plotted the relative analyte-induced variations of the calculated resistance and capacitance in Figure 7e. As one can see, there is a good coincidence of the results with the data depicted in Figures 4c and 7c. A small difference between experimental sensor response shown in Figure 4c and the relative variation of resistance shown in Figure 7e, is observed for butanol as compared to ammonia. This could be related to the competitive hydrogen bonds formation, which is much stronger in case of NH₃ as compared with butanol molecules. Overall, the resistance's variation induced by an H₂O molecule, about 18%, remarkably exceeds the ones exhibited by other analytes. At the same time, the quantum capacitance varies in 2%-range. This supports that the observed chemiresistive effect in the 2D Mo₂C structure is primarily governed by the surface receptor's function.

3. Conclusions

The study presents a promising way to develop a chemiresistive-type hygrometer employing the 2D flakes of Mo₂CT_x MXenes derived from layered Mo₂Ga₂C transition metal carbide precursors. We have found that the humidity vapors enhance the resistance of the poly-flake Mo₂CT_x layer with a high SNR value which allows for the reversible detection at least down to 10 ppm of H₂O. The upper detection limit is at least 10 000 ppm in humid air thus covering a dynamic range of 3 decades. Furthermore, we demonstrate that the material's selectivity to different vapors could be approached by designing an on-chip multisensor array where the vector signal is calibrated versus other possible analytes along the Electronic nose concept. The supported measurements of the ac impedance in these 2D structures combined with DFT calculations prove the observed effect to be governed primarily by the H₂O-induced variation of resistivity. The DFT data are in good agreement with the experiments regarding the resistance and capacitance variations, as well as supporting the reversible character of H₂O adsorption and other organic vapors over the material's surface. We suggest that the observed performance of Mo₂CT_x meets many possible applications which consider the hygrometry as a required tool and paths the way for applications of Mo₂CT_x MXenes.

4. Experimental Section

The synthesis procedure of the Mo₂Ga₂C precursor was similar to protocols reported earlier.^[37] Briefly, gallium pieces (Ga, ≈99.5%) were manually mixed with molybdenum carbide powder (Mo₂C, ≈99.5%, ≈325 mesh) in a stoichiometric ratio of 8:1 using a mortar and a pestle until forming a homogenous paste. Afterward, the paste was placed in a quartz tube, which was evacuated and sealed. The sealed tube was transferred to a horizontal tube furnace and heated up to 850 °C

at 10 °C min⁻¹ with a dwell time of 48 h, and afterward cooled down to RT in an inert mode. After sintering, the produced compact was grinded, placed back in a quartz tube and reheated in a tube furnace to 850 °C at a rate of ≈10 °C min⁻¹, and successively held for additional 12 h. After cooling down to RT the sintered powders were grinded. 1 g of synthesized Mo₂Ga₂C nanolaminated carbide powder, of particle sizes to be less than 25 μm, was gently added to 20 mL of hydrofluoric acid, HF, (48%, Sigma-Aldrich) and continuously stirred for 7 days at 55 °C. After chemical etching, the suspension was washed in the water of high purity via repeated centrifuging (Eppendorf Centrifuge 5804, Germany) at 3500 rpm for 5 min until the pH of the residue solution was close to 5–6. The obtained multilayer powder was further delaminated with tetrabutylammonium hydroxide, TBAOH, (40 wt% in H₂O, Sigma-Aldrich). For this purpose, the 3 mL of TBAOH was added to multilayer Mo₂CT_x powder and the obtained mixture was sonicated for 1 h at 100 W power. After the delamination, the suspension was washed with the absolute ethanol via centrifugation at 3500 rpm for 5 min until neutral pH was reached. To collect the delaminated Mo₂CT_x flakes, the slurry was dispersed in the distilled water and was subjected to final centrifugation for 30 min at 3500 rpm. The produced black stable solution was vacuum filtered, dried, and stored in an inert atmosphere prior to further use.

The nanolaminated molybdenum carbide precursor and multilayer MXene powder were characterized using X-ray diffraction (Malvern Panalytical X'Pert MPD PW3040 Diffractometer) operating in Bragg–Brentano geometry (0.001° goniometer resolution). Nonmonochromatized X-rays with Cu anode and a weighted average wavelength of 1.5418 Å were used. The XRD patterns were collected in the range of 2θ = 5–60° with a step of 0.01° and were processed with HighScore Plus software. For the transmission electron microscopy (TEM) studies, delaminated and diluted Mo₂CT_x MXene aqueous suspension was drop cast on a lacey carbon film on 300 mesh copper grid (Plano GmbH, Germany) and left for 20 min to air dry. Bright-field (BF) images and selected area electron diffraction (SAED) patterns were acquired with an FEI Tecnai F20 transmission electron microscope (FEI Comp., The Netherlands) at an acceleration voltage of 200 kV. The phase analysis was carried out using Gatan Microscopy Suite software. Topography and height profile of delaminated Mo₂CT_x flakes deposited on Si/SiO₂ substrates was performed using atomic force microscopy on NTEGRA SPECTRA System. HR-XPS and valence band spectra were collected at the VUV-Photoemission beamline of the synchrotron Elettra (Trieste, Italy).

As a test platform for the sensor prototyping, the Si/SiO₂ substrate, 0.4 mm thick, equipped with Pt metallization, ≈1 μm thick, to form at the front side multiple strip electrodes, each of 4.3 mm length and 50 μm width, which frame the sensor area of 0.215 mm² square were employed. Each electrode ends at the chip side with a contact pad of ≈0.036 mm² for further wiring. The interelectrode gap which confines the sensing material under study is 46–50 μm due to the trapezoid shape of the electrodes. Each two-electrode area is considered as a single chemiresistor, while the total set number of these sensors forms the multisensor array in the chip. The two meander couples of thermoresistors and heaters are placed at both sides of the chip area to manage and control the chip's operating temperature. The total chip is squared to be ≈10 × 9 mm². The chip is wired by Au wires, of 38 μm diameter, by ultrasound (WEST Bond 747677E, USA) into the ceramic holder supplied with the 50-pin connector, 1.27 mm pitch (ERNI Electronics GmbH & Co. KG, Germany) to be interfaced to external reading electronic circuits.

The aqueous suspension of Mo₂CT_x flakes of 0.25 wt% has been dropped at the volume of 2 mL over the chip surface and was subject to drying in air at 60 °C for few minutes. The morphology of the film surface has been inspected with SEM (Tescan Vega 3SB, Czech Republic) at 20 keV of accelerating voltage. The elemental composition over the surface was checked and mapped with SEM in-built silicon drift detector, 10 mm² (X-act, Oxford Instruments Inc.) at 125 eV energy resolution.

The Mo₂CT_x layer thickness at the chip has been evaluated by means of a stylus profiler (Dektak 150, Veeco, USA) with a stylus radius of 2 μm to be forced at 1 mg; the measuring point resolution has been installed

at $\approx 0.05 \mu\text{m}$. The profiles have been measured over pristine chip substrates without the Mo_2CT_x layer as a reference in various parts to cross the chip. The Mo_2CT_x -covered chip has been profiled in the same manner to be compared with the pristine surface.

For gas-sensing measurements, the chip has been placed into a sealed steel chamber, of $\approx 0.2 \text{ cm}^3$ of internal volume, containing input and output tubes for a test gas flow through the chip so that the chip front side faces the incoming gaseous analyte's probes. The chamber and connecting wires are placed into the grounded Faraday box to ensure stable electric measurements, free of external electromagnetic interferences. The chemiresistive signal of each sensor located at the chip has been measured via recording a dc current with current preamplifier (SR570, Stanford amplifier, USA) under the electric bias of 1 V applied across each couple of the electrodes by analog input–output unit (USB-6259, National Instruments, USA). The reading electronics allow one to measure the resistances in the range from Ohms to tens GOhms. The relay multiplexing cards (SRD-05VDC-SL-C, Songle Relay, China) ensure measuring all the sensors in the array in a sequence. The minimum reading rate is limited by a time RC-constant to ensure proper resistance reading; here, the rate was 0.3–0.7 ms per sensor under multiplexing. The I – V curves were measured by application of dc electric bias to each sensor electrodes of the array in the range of $[-1; +1]$ V in forward and backward directions to ensure repeatability. All the setup has been managed by a personal computer with homemade software.

The analyte gases have been supplied to the chip surface in a flow mode. To make the probes, the background lab air has been pumped into the gas delivery system by a compressor (Precision Compressed Air 230v, Peak Scientific Instruments Ltd., UK) upon 2 atm pressure to be further dried down to below 200 pm of residual humidity and mechanically filtered with a dry air generator (Purge PG14L, Peak Scientific, UK). This dry air has been employed as a reference in all the measurements. The humidity vapors and other analytes of alcohols, acetone, and ammonia of analytical grade were supplied primarily in a liquid phase: distilled water, alcohols to be 95.6 rel% solutions, acetone to be 99 rel% solutions, and 25% NH_4 solution in the water. The reference air has been bubbled through the corresponding liquids to be enriched with the analytes, of the saturation partial pressure managed primarily the lab temperature, under a varied flow rate driven by PC with high-precision mass-flow controllers (Bronkhorst, Netherlands). The analyte probes with varied concentrations, 10^1 – 10^4 ppm range, in mixture with air were generated by forking the pure air and analyte-enriched air in various flow ratios to keep the same overall flow rate in all the measurements at 400 sccm. The analyte measurements in a wet air were installed by mixing the analyte-enriched flow with air/ H_2O , 25 rel%, mixture flow at the same concentration range. All the tubes, of 1/4" diameter, were confidently connected in the setup by Swagelok fittings. The humidity content in the gas flow was independently verified with a commercial capacitive sensor (AM2302, Guangzhou Aosong Electronics Co, China) which also indicated the presence of other analytes being rather unselective. In experiments, the chip exposure to analytes has been conducted for 1 h with further purging by pure air, dry or wet one as a reference, for 2 h at least.

Most measurements of the chemiresistive response of the Mo_2CT_x layer have been conducted at room temperature which has varied in the 28–35 °C range in dependence on laboratory conditions. Some data were recorded when the chip was heated up to 100 °C employing a PID controller (Elhart ECD2-M-CC-RS, KIP-service, Russia) to drive the current via meander heaters located at the chip. The thermoresistor values have served as feedback following a proper calibration with IR camera (InfRec R500EX-P-D, NIPPON AVIONICS CO. LTD, Japan) equipped with a macro lens (21 μm Close-Up Lens, IRL-C021UB20, Japan). The IR images of the chip under various heating were acquired at -40 – $+120$ °C range mode of IR camera and processed by NS9500PRO software.

To perform the ac excitation of the electric field to the Mo_2CT_x layer, the chip has been installed to the sealed chamber and measured with impedance meter (Alpha-A Novocontrol, Novocontrol Technologies GmbH & Co. KG, Germany) in ac frequency's range of 10^{-2} – 10^6 Hz. The impedance of the Mo_2CT_x layer confined between a couple of

electrodes has been read out in dry air flow and humidity-enriched air, of 25 rel%, flow, equal to 400 sccm similar to the basic dc chemiresistive measurements. The parameters of equivalence circuits were built employing $Z(f)$ curves with Z-View software (Ametec Inc., USA).

The vector signal of the multisensor array located at the chip has been processed by LDA algorithm using homemade software to selectively discriminate the analytes under study. To feed the LDA processing, the dc resistance values of the sensors, R_i , recorded upon exposure to various analyte probes were employed when the $R(t)$ transient pass over the fast variation induced by a gas's change in the chamber.

The search for equilibrium atomic configurations of Mo_2C supercells was carried out with help of the DFT implemented in the SIESTA software package^[70,71] under applying DZP (double- ζ -polarized) basis which includes polarization functions. The program employs a finite grid in a coordinate space to calculate integrals and to represent charge densities and potentials. The rate and accuracy of the calculations are defined by the value of cutting plane waves (Mesh Cut off), which is externally set out. The trade-off between the rate and accuracy is the value of 350 Ry which is used in most systems consisting of no more than a thousand atoms. To relax the geometry of the structure, the $24 \times 1 \times 1$ set of k -points was taken using the Monkhorst-Pack scheme when sampling the Brillouin zone.^[72] The convergence conditions of the geometry optimization were set at an atomic force to be smaller than $10^{-3} \text{ eV } \text{\AA}^{-1}$. To perform the geometric optimization of the crystal lattice and its tetragonal distortion, the "smearing" and "tetrahedra" modes were utilized, respectively. To take into account an electron-ion interaction, the projection augmented wave (PAW) method was applied. The exchange-correlation interaction was described in the generalized gradient approximation (GGA) under the PBE (Perdew–Burke–Ernzerhof) parameterization.^[73] The interaction of the surface with analyte molecules was approached with van-der-Waals density functional (vdW-DF) approximation employing the exchange-correlation functional by Berland and Hyldgaard (BH).^[74] This BH functional has been already used both to calculate the topology of the structure and quantum transport of electrons.^[75,76]

To calculate the chemiresistive response of the Mo_2C supercell, the electrical resistances were calculated before and after the analyte's adsorption. For this purpose, TranSIESTA software was employed which calculates the electronic structure formed by a finite subsystem under study sandwiched between a couple of conducting electrodes. The TranSIESTA method closely relates to the SIESTA code because the TranSIESTA calculations involve finding the electron density from the DFT Hamiltonian using Green's functions instead of the ordinary diagonalization procedure. The calculation of transport properties accounts for the electrodes and scattering regions within the system under study. The calculation of TranSIESTA for the scattering region primarily employs the conventional SIESTA procedure which generates a density matrix using the Kohn–Sham scheme for periodic systems. In the SIESTA code, the transmission function has been calculated by in-built TBtrans software.

Supporting Information

Supporting Information is available from the Wiley Online Library or from the author.

Acknowledgements

This work has been partially funded through the project EUROFEL-ROADMAP ESFRI. D.A.K. thanks RFBR, project No. 19-32-90160, for the partial support of the DFT calculations. This work was supported by the Deutsche Forschungsgemeinschaft (DFG) within CRC/TRR 270, project B02 (Project-ID 405553726). Authors thank Prof. V. Goffman (SSTU) for a support with impedance meter measurements.

Open access funding enabled and organized by Projekt DEAL.

Conflict of Interest

The authors declare no conflict of interest.

Data Availability Statement

The data that support the findings of this study are available from the corresponding author upon reasonable request.

Keywords

alcohol, chemiresistor, DFT, humidity, Mo₂CT_x, multisensor array, vdW-DF

Received: June 25, 2021

Revised: September 7, 2021

Published online: October 19, 2021

- [1] S. Yang, C. Jiang, S.-h. Wei, *Appl. Phys. Rev.* **2017**, *4*, 021304.
- [2] L. Zhang, K. Kahn, J. Zou, H. Zhang, Y. Li, *Adv. Mater. Interfaces* **2019**, *6*, 1901329.
- [3] D. J. Buckley, N. C. G. Black, E. G. Castanon, C. Melios, M. Hardman, O. Kazakova, *2D Mater.* **2020**, *7*, 032002.
- [4] K. Deshmukh, T. Kovářík, S. K. K. Pasha, *Coord. Chem. Rev.* **2020**, *424*, 213514.
- [5] F. Schedin, A. K. Geim, S. V. Morozov, E. W. Hill, P. Blake, M. I. Katsnelson, K. S. Novoselov, *Nat. Mater.* **2007**, *6*, 652.
- [6] R. Kumar, N. Goel, M. Hojamberdiev, M. Kumar, *Sens. Actuators, A* **2020**, *303*, 111875.
- [7] S. Angizi, M. Khalaj, S. A. A. Alem, A. Pakdel, M. Willander, A. Hatamie, A. Simchi, *J. Electrochem. Soc.* **2020**, *167*, 126513.
- [8] Y. Li, A.-S. Xiao, B. Zou, H.-X. Zhang, K.-L. Yan, Y. Lin, *Polyhedron* **2018**, *154*, 83.
- [9] S. Cui, H. Pu, S. A. Wells, Z. Wen, S. Mao, J. Chang, M. C. Hersam, J. Chen, *Nat. Commun.* **2015**, *6*, 8632.
- [10] M. Li, J. Lu, K. Luo, Y. Li, K. Chang, K. Chen, J. Zhou, J. Rosen, L. Hultman, P. Eklund, P. O. Å. Persson, S. Du, Z. Chai, Z. Huang, Q. Huang, *J. Am. Chem. Soc.* **2019**, *141*, 4730.
- [11] V. Kamysbayev, A. S. Filatov, H. Hu, X. Rui, F. Lagunas, D. Wang, R. F. Klie, D. V. Talapin, *Science* **2020**, *369*, 979.
- [12] S. M. Aghaei, A. Aasi, B. Panchapakesan, *ACS Omega* **2021**, *6*, 2450.
- [13] E. Lee, D.-J. Kim, *J. Electrochem. Soc.* **2020**, *167*, 037515.
- [14] M. Naguib, V. N. Mochalin, M. W. Barsoum, Y. Gogotsi, *Adv. Mater.* **2014**, *26*, 992.
- [15] D. H. Ho, Y. Y. Choi, S. B. Jo, J.-M. Myoung, J. H. Cho, *Adv. Mater.* **2021**, 2005846, <https://doi.org/10.1002/adma.202005846>.
- [16] Y. Pei, X. Zhang, Z. Hui, J. Zhou, X. Huang, G. Sun, W. Huang, *ACS Nano* **2021**, *15*, 3996.
- [17] E. Lee, A. VahidMohammadi, B. C. Prorok, Y.-S. Yoon, M. Beidaghi, D.-J. Kim, *ACS Appl. Mater. Interfaces* **2017**, *9*, 37184.
- [18] W. Yuan, K. Yang, H. Peng, F. Li, F. Yin, *J. Mater. Chem. A* **2018**, *6*, 18116.
- [19] S.-J. Kim, H.-J. Koh, C. E. Ren, O. Kwon, K. Maleski, S.-Y. Cho, B. Anasori, C.-K. Kim, Y.-K. Choi, J. Kim, Y. Gogotsi, H.-T. Jung, *ACS Nano* **2018**, *12*, 986.
- [20] M. Wu, M. He, Q. Hu, Q. Wu, G. Sun, L. Xie, Z. Zhang, Z. Zhu, A. Zhou, *ACS Sens.* **2019**, *4*, 2763.
- [21] H.-J. Koh, S. J. Kim, K. Maleski, S.-Y. Cho, Y.-J. Kim, C. W. Ahn, Y. Gogotsi, H.-T. Jung, *ACS Sens.* **2019**, *4*, 1365.
- [22] Y. Chae, S. J. Kim, S.-Y. Cho, J. Choi, K. Maleski, B. J. Lee, H.-T. Jung, Y. Gogotsi, Y. Lee, C. W. Ahn, *Nanoscale* **2019**, *11*, 8387.
- [23] H. Pazniak, I. A. Plugin, M. J. Loes, T. M. Inerbaev, I. N. Burmistrov, M. Gorshenkov, J. Polcak, A. S. Varezhinov, M. Sommer, D. V. Kuznetsov, M. Bruns, F. S. Fedorov, N. S. Vorobeva, A. Sinitkii, V. V. Sysoev, *ACS Appl. Nano Mater.* **2020**, *3*, 3195.
- [24] H. Tai, Z. Duan, Z. He, X. Li, J. Xu, B. Liu, Y. Jiang, *Sens. Actuators, B* **2019**, *298*, 126874.
- [25] Y. Gogotsi, Q. Huang, *ACS Nano* **2021**, *15*, 5775.
- [26] J. Halim, S. Kota, M. R. Lukatskaya, M. Naguib, M.-Q. Zhao, E. J. Moon, J. Pitcock, J. Nanda, S. J. May, Y. Gogotsi, M. W. Barsoum, *Adv. Funct. Mater.* **2016**, *26*, 3118.
- [27] Z. W. She, K. D. Fredrickson, B. Anasori, J. Kibsgaard, A. L. Strickler, M. R. Lukarskaya, Y. Gogotsi, T. F. Jaramillo, A. Vojvodic, *ACS Energy Lett.* **2016**, *1*, 589.
- [28] J. Mei, G. A. Ayoko, C. Hu, J. M. Bell, Z. Sun, *Sustainable Mater. Technol.* **2020**, *25*, e00156.
- [29] W. Guo, S. G. Surya, V. Babar, F. Ming, S. Sharma, H. N. Alshareef, U. Schwingenschlögl, K. N. Salama, *ACS Appl. Mater. Interfaces* **2020**, *12*, 57218.
- [30] Q.-N. Zhao, Y.-J. Zhang, Z.-H. Duan, S. Wang, C. Liu, Y.-D. Jiang, H.-L. Tai, *Rare Met.* **2021**, *40*, 1459.
- [31] Z. Yang, A. Liu, C. Wang, F. Liu, J. He, S. Li, J. Wang, R. You, X. Yan, P. Sun, Y. Duan, G. Lu, *ACS Sens.* **2019**, *4*, 1261.
- [32] H. An, T. Habib, S. Shah, H. Gao, A. Patel, I. Echols, X. Zhao, M. Radovic, M. J. Green, J. Lutkenhaus, *ACS Appl. Nano Mater.* **2019**, *2*, 948.
- [33] J. Wu, P. Lu, J. Dai, C. Zheng, T. Zhang, W. W. Yu, Y. Zhang, *Sens. Actuators, B* **2021**, *326*, 128969.
- [34] L. Wang, M. Tian, Y. Zhang, F. Sun, X. Qi, Y. Liu, L. Qu, *J. Mater. Sci.* **2020**, *55*, 6187.
- [35] Z. Wang, K. Yu, Y. Feng, R. Qi, J. Ren, Z. Zhu, *Appl. Surf. Sci.* **2019**, *496*, 143729.
- [36] F. M. Römer, U. Wiedwald, T. Strusch, J. Halim, E. Mayerberger, M. W. Barsoum, M. Farle, *RSC Adv.* **2017**, *7*, 13097.
- [37] C. Hu, C.-C. Lai, Q. Tao, J. Lu, J. Halim, L. Sun, J. Zhang, J. Yang, B. Anasori, J. Wang, Y. Sakka, L. Hultman, P. Eklund, J. Rosen, M. W. Barsoum, *Chem. Commun.* **2015**, *51*, 6560.
- [38] P. S. Gromski, A. B. Henson, J. M. Granda, L. Cronin, *Nat. Rev. Chem.* **2019**, *3*, 119.
- [39] T. Wang, D. Huang, Z. Yang, S. Xu, G. He, X. Li, N. Hu, G. Yin, D. He, L. Zhang, *Nano-Micro Lett.* **2016**, *8*, 95.
- [40] D. Gu, S. K. Dey, *Appl. Phys. Lett.* **2006**, *89*, 082907.
- [41] E. Lucazeau, A. Deneuille, J. Fontenille, F. Brunet, E. Gheeraert, *Diamond Relat. Mater.* **1996**, *5*, 779.
- [42] H. Farahani, R. Wagiran, M. N. Hamidon, *Sensors* **2014**, *14*, 7881.
- [43] Y. Zhang, Y. Jiang, Z. Duan, Q. Huang, Y. Wu, B. Liu, Q. Zhao, S. Wang, Z. Yuan, H. Tai, *Sens. Actuators, B* **2021**, *344*, 130150.
- [44] J. Li, Z. Chi, R. Qin, L. Yan, X. Lin, M. Hu, G. Shan, H. Chen, Y.-X. Weng, *J. Phys. Chem. C* **2020**, *124*, 10306.
- [45] J. A. B. Da Silva, F. G. B. Moreira, V. M. L. Dos Santos, R. L. Longo, *Phys. Chem. Chem. Phys.* **2011**, *13*, 6452.
- [46] G. Korotcenkov, V. Brinzari, B. K. Cho, in *Chemical Sensors: Comprehensive Sensor Technologies. Vol. 4. Solid State Devices* (Eds: G. Korotcenkov), Momentum Press, New York **2011**, pp. 53–186.
- [47] V. V. Sysoev, E. Strelcov, A. Kolmakov, in *Metal Oxide Nanomaterials for Chemical Sensors* (Eds: M. Carpenter, S. Mathur, A. Kolmakov), Springer, New York **2013**, pp. 465–502.
- [48] R. Henrion, G. Henrion, *Multivariate Datenanalyse*, Springer, Berlin **1995**.
- [49] A. Lipatov, A. Varezchnikov, P. Wilson, V. Sysoev, A. Kolmakov, A. Sinitkii, *Nanoscale* **2013**, *5*, 5426.
- [50] J. van den Broek, S. Abegg, E. Pratsinis, A. T. Güntner, *Nat. Commun.* **2019**, *10*, 4220.

- [51] V. V. Sysoev, I. Kiselev, V. Trouillet, M. Bruns, *Sens. Actuators, B* **2013**, *185*, 59.
- [52] A. D'Amico, C. Di Natale, *IEEE Sens. J.* **2001**, *1*, 183.
- [53] X.-H. Zha, J. Yin, Y. Zhou, Q. Huang, K. Luo, J. Lang, J. S. Francisco, J. He, S. Du, *J. Phys. Chem. C* **2016**, *120*, 15082.
- [54] E. S. Muckley, M. Naguib, I. N. Ivanov, Multi-Modal, *Nanoscale* **2018**, *10*, 21689.
- [55] N. Li, Y. Jiang, C. Zhou, Y. Xiao, B. Meng, Z. Wang, D. Huang, C. Xing, Z. Peng, *ACS Appl. Mater. Interfaces* **2019**, *11*, 38116.
- [56] E. S. Muckley, M. Naguib, H.-W. Wang, L. Vlcek, N. C. Osti, R. L. Sacci, X. Sang, R. R. Uocic, Y. Xie, M. Tyagi, E. Mamontov, K. L. Page, P. R. C. Kent, J. Nanda, I. N. Ivanov, *ACS Nano* **2017**, *11*, 11118.
- [57] X. Zhao, L.-Y. Wang, C.-Y. Tang, X.-J. Zha, Y. Liu, B.-H. Su, K. Ke, R.-Y. Bao, M.-B. Yang, W. Yang, *ACS Nano* **2020**, *14*, 8793.
- [58] L.-X. Liu, W. Chen, H.-B. Zhang, Q.-W. Wang, F. Guan, Z.-Z. Yu, *Adv. Funct. Mater.* **2019**, *29*, 1905197.
- [59] P. He, J. R. Brent, H. Ding, J. Yang, D. J. Lewis, P. O'Brien, B. Derby, *Nanoscale* **2018**, *10*, 5599.
- [60] F. S. Fedorov, A. S. Varezchnikov, I. Kiselev, V. V. Kolesnichenko, I. N. Burmistrov, M. Sommer, D. Fuchs, C. Kübel, A. V. Gorokhovskiy, V. V. Sysoev, *Anal. Chim. Acta* **2015**, *897*, 81.
- [61] J. T. S. Irvine, D. C. Sinclair, A. R. West, *Adv. Mater.* **1990**, *2*, 132.
- [62] A. K. Jonscher, *Nature* **1977**, *267*, 673.
- [63] S. Kumari, N. Ortega, A. Kumar, S. P. Pavunni, J. W. Hubbard, C. Rinaldi, G. Srinivasan, J. F. Scott, R. S. Katiyar, *J. Appl. Phys.* **2015**, *117*, 114102.
- [64] G. E. Pike, *Phys. Rev. B* **1972**, *6*, 1572.
- [65] J. Li, T. Joseph, M. Ghorbani-Asl, S. Kolekar, A. V. Krashennnikov, M. Batzill, *Nanoscale* **2021**, *13*, 1038.
- [66] G. Levita, P. Restuccia, M. C. Righi, *Carbon* **2016**, *107*, 878.
- [67] A. Michaelides, *Appl. Phys. A* **2006**, *85*, 415.
- [68] L. R. Merte, R. Bechstein, G. Peng, F. Rieboldt, C. A. Faberow, H. Zeuthen, J. Knudsen, E. Lægsgaard, S. Wendt, M. Mavrikakis, F. Besenbacher, *Nat. Commun.* **2014**, *5*, 4193.
- [69] Q. Xu, G. M. Yang, W. T. Zheng, *Mater. Today Commun.* **2020**, *22*, 100772.
- [70] J. M. Soler, E. Artacho, J. D. Gale, A. García, J. Jungquera, P. Ordejón, D. Sánchez-Portal, *J. Phys.: Condens. Matter* **2002**, *14*, 2745.
- [71] A. García, N. Papior, A. Akhtan, E. Artacho, V. Blum, E. Bosoni, P. Brandimarte, M. Brandbyge, J. I. Cerdá, F. Corsetti, R. Cuadrado, V. Dikan, J. Ferrer, J. Gale, P. García-Fernández, V. M. García-Suárez, S. García, G. Huhs, S. Illera, R. Korytár, P. Koval, I. Lebedeva, L. Lin, P. López-Tarifa, S. G. Mayo, S. Mohr, P. Ordejón, A. Postnikov, Y. Pouillon, M. Pruneda, R. Robles, D. Sánchez-Portal, J. M. Soler, R. Ullah, V. W.-z. Yu, J. Junquera, *J. Chem. Phys.* **2020**, *152*, 204108.
- [72] H. J. Monkhorst, J. D. Pack, *Phys. Rev. B* **1976**, *13*, 5188.
- [73] J. P. Perdew, K. Burke, M. Ernzerhof, *Phys. Rev. Lett.* **1996**, *77*, 3865.
- [74] K. Berland, P. Hyldgaard, *Phys. Rev. B* **2014**, *89*, 035412.
- [75] K. Berland, V. R. Cooper, K. Lee, E. Schröder, T. Thonhauser, P. Hyldgaard, B. I. Lundqvist, *Rep. Prog. Phys.* **2015**, *78*, 066501.
- [76] P. Hyldgaard, Y. Jiao, V. Shukla, *J. Phys.: Condens. Matter* **2020**, *32*, 393001.